Science and Technology Indonesia
e-ISSN:2580-4391 *p*-ISSN:2580-4405
Vol. 11, No. 1, January 2026

Research Paper

Enhancing Scattering Strength Improvement and Color Uniformity in White Light-Emitting Diodes Using High Concentration of Yttrium Oxide

Pham Hong Cong[1], Nguyen Thi Phuong Loan[2]*, Ha Thanh Tung[3]

[1]*Faculty of Electrical Engineering Technology, Industrial University of Ho Chi Minh City, Ho Chi Minh City, 70000, Vietnam*
[2]*Faculty of Fundamental 2, Posts and Telecommunications Institute of Technology, Ho Chi Minh City, 70000, Vietnam*
[3]*Faculty of Basic Sciences, Vinh Long University of Technology Education, Vinh Long Province, 85000, Vietnam*
***Corresponding author**: ntploan@ptithcm.edu.vn

Abstract
This study investigates the effect of yttrium oxide (Y_2O_3) doping on the phase evolution of barium titanate ($BaTiO_3$), a key dielectric material used in multilayer ceramic capacitors (MSCCs). Two types of starting powders were examined: pure $BaTiO_3$ and a commercial X7R composition containing 1 wt% Y_2O_3. Using the solid-state method under high temperature, Y_2O_3 was added in varying amounts, and the powders were processed under controlled sintering conditions to evaluate its influence on phase formation. The resulting ceramics were characterized to determine formational alterations as well as the potential generation of secondary phases. Increasing Y_2O_3 content led to a transmutation from the tetragon structure to a merger between tetragon as well as cubic phases. The commercial X7R powder exhibited greater densificating process, surpassing pure $BaTiO_3$ and formed a cuboid formation under greater Y_2O_3 concentrations. Notably, the sample doped with 20 wt% Y_2O_3 produced the $Ba_6Ti_{17}O_{40}$ phase, augmenting scattering capacity and color uniformity. These findings clarify the role of Y_2O_3 in phase evolution and highlight its implications for optimizing $BaTiO_3$-based MSCC materials.

Keywords
YAG:Ce^{3+}, LEDs, Lumen Output, Color Quality, Y_2O_3

Received: 16 August 2025, Accepted: 29 October 2025
https://doi.org/10.26554/sti.2026.11.1.174-181

1. INTRODUCTION

Barium titanate ($BaTiO_3$) has long been recognized as one of the most widely utilized dielectric substances within multi-sheet ceramic capacitor (MSCCs) units for its significant dielectric constant, excellent ferroelectric properties, and unique electromagnetic behavior (Anh and Ngoc, 2020; Thi et al., 2020). However, in practical applications, MSCCs are often exposed to elevated temperatures and high electric fields, conditions under which the dielectric stability of $BaTiO_3$ becomes a critical factor (Loan and Anh, 2021; That et al., 2020). To address these challenges, various doping strategies and additive modifications have been explored to tune the structural, electrical, and thermal stability of $BaTiO_3$-based ceramics (Rianjanu et al., 2025; Thuy et al., 2025). Common approaches include the incorporation of transition-metal dopants such as Mn, Mg, and Ca, which act as compensators for charge carriers generated by oxygen vacancies (Dang et al., 2021a). In addition, sintering aids like SiO_2 have been introduced to lower the eutectic point through the formation of a BaO-TiO_2-SiO_2 ternary system, thereby enhancing densification during processing (Thi et al., 2021). Another widely applied modification involves rare-earth element (REE) doping, in which cations such as Dy^{3+}, Ho^{3+}, Sm^{3+}, La^{3+}, Yb^{3+}, snd Y^{3+} substitute Ba^{2+} or Ti^{4+} sites within the BaTiO3 lattice (Thi et al., 2021). These dopants have been shown to influence both the microstructural evolution and the long-term reliability of MSCCs, with certain ions like Dy^{3+}, Ho^{3+}, and Y^{3+} exhibiting amphoteric behavior beneficial for dielectric stability. Among these, Y_2O_3 has attracted significant attention due to its relatively low cost, commercial availability, and performance comparable to that of other REE dopants (Cong and Anh, 2025; Hadi et al., 2025). Indeed, Y^{3+} doping is already extensively used in industrial formulations of $BaTiO_3$ powders.

The mechanism by which Yb^{3+} interacts with the $BaTiO_3$ lattice is of particular interest. Owing to its ionic radius, Yb^{3+} can substitute at either Ba^{2+} or Ti^{4+} sites, acting as an acceptor or donor depending on the site occupancy. This substitution process is strongly influenced by processing conditions such as oxygen partial pressure, sintering atmosphere, dopant concentration, and the Ba/Ti ratio. Previous studies have demonstrated that the solubility limit of Yb^{3+} varies widely depending

on the site (Pham et al., 2021). Beyond these solubility thresholds, secondary phases such as $Ba_6Ti_{17}O_{40}$ and $Y_2Ti_2O_7$ may precipitate, which have been associated with adverse effects on the dielectric reliability of $BaTiO_3$-based MSCCs (Dang et al., 2021b).

Most industrial formulations employ relatively low doping concentrations (<1 wt%) and sintering under reducing conditions to suppress defect formation and stabilize desired microstructures (Dang et al., 2021c; That and Anh, 2021). By contrast, the novelty of the present work concerns systematically investigating the effect from high Y_2O_3 doping levels (>1 wt%) under air-sintering conditions. This approach enables us to explore the influence of excessive dopant concentrations, well beyond the conventional solubility limits, on the structural evolution, phase stability, and defect chemistry of $BaTiO_3$. In doing so, we aim to provide deeper insights into the mechanisms governing dopant incorporation and secondary phase formation, thereby extending current understanding of $BaTiO_3$ modification strategies and offering new perspectives for the design of high-performance dielectric ceramics.

2. EXPERIMENTAL SECTION

2.1 Materials

A powder of $BaTiO_3$ doped with Y_2O_3 (with a structure of $Ba_{1-x}Y_xTi_{1-x/4}O_3$) was produced using a typical solid-state process. Two kinds of barium titanate ($BaTiO_3$) were employed: "BT-A" (commercial reagent-grade, ≥99%, Sigma-Aldrich) and "BT-B" (designed for MSCC manufacture, containing additional substances. Yttrium oxide (Y_2O_3, ≥99.9%, Sigma-Aldrich) was used as a dopant. Polyvinyl butyral (PVB, M.W. 50,000, Sigma-Aldrich) was used as a binder. Every chemical was acquired and utilized with no additional refinement.

2.2 Synthesis

10 g of $BaTiO_3$ powder (BT-A or BT-B) was mixed with Y_2O_3 to obtain doping levels of 2.5, 5, 10, 15, and 20 wt%. Powders were ball-milled in a 250 mL polyurethane milling container via zirconia beads (10 mm diameter) in a weight ratio of 1:10 (powder:balls) for 12 h at 300 rpm to achieve homogeneous mixing (Alaizeri et al., 2025). After milling, the powders were desiccated under 80 °C within 12 h inside an oven. This step ensured complete removal of moisture and improved powder flow during ceramic fabrication (Ma et al., 2025). Dried powders doped with 2.5 and 5 wt% Y_2O_3 were mixed with 1 wt% PVB, ground manually for 30 min, and sieved through a 200-mesh sieve. Powders were then uniaxially pressed into 8 mm discs at a pressure of 200 MPa (Hou et al., 2025). Sintering was carried out in air at 1300 °C within 4 h under a firing/chilling pace reaching 5 °C per minute.

2.3 Characterization

Powder and sintered specimens were analyzed using X'Pert PRO XRD with Cu Kα radioactivity (λ = 1.5418 Å), operating under 40 kV and 30 mA. Scanning instances were carried out over 2θ scope 10–80° under a step magnitude reaching 0.02° as well as a scanning pace of 0.5° per minute. Crystallite magnitudes were approximated via the full width at half maximum (FWHM) of main diffractive peaks utilizing the Scherrer formula. Powder morphology and sintered surfaces were examined using a Tescan Lyra SEM at an accelerating voltage of 15 kV (Li et al., 2019, 2018). Figure 1 displays the characterization data for the specimens acquired by XRD in Figure 1(a) and SEM in Figure 1(b). Samples were mounted on carbon-conductive tape then daubed using one thin gold sheet (5 nm) for preventing charging. Granule magnitudes were identified via SEM images utilizing ImageJ application, with more than 100 granules identified for all samples. Bulk denseness (ρ) for sintered ceramic units was calculated via the measured weight as well as dimensions of the discs using (Limbu et al., 2020; Lissner and Urban, 2011):

$$\rho = \frac{\text{mass}}{\text{volume}}$$

Each measurement was repeated three times, and the average value was reported. All experiments were repeated three times to ensure reproducibility. Milling, pressing, and sintering conditions were kept identical across all samples to allow reliable comparison of the effect of Y_2O_3 doping.

3. RESULTS AND DISCUSSION

SEM pictures of the undoped $BaTiO_3$ powders, A0 and B1, reveal particles having coarse-faceted structure. Two particle dimensions were found: 0.48 μm to 1.25 μm for the A0 and 0.46 μm to 0.81 μm for the B1. While the outcomes prove similar, the highest mean number for the B1 granules would be inferior to the A0 counterparts, caused by the heat processing applied to the formed powder in the form of a component in the MSCCs manufacturing procedure (Liu et al., 2012; Shi et al., 2023).

The X-ray diffracting structures for the heated powder are given. The powder diffracting structures produced from the BT-A were consistent with the tetragonal stage. It displays the highest points linked to the (111) and (002)(200) planes of this stage. The diffracting maximum at 2θ around 45° splits into two maxima, indicating a tetragon state. Regarding the A20 powder, the planes (002) and (200) are slightly distorted, while the plane (111) changes towards a lesser angle. Furthermore, according to A5 as well as A20 specimens, maxima that correspond to Y_2O_3 show, showing that at least some of it stays free exterior of the $BaTiO_3$ structure, showing that the soluble ability threshold has been exceeded. The change to lower angles of some maxima is a result of a growth of the unit cell volume caused by a replacement of Ba^{2+} ions with Y^{3+}.

The XRD structures of BT-B powder alter more with rising Y_2O_3 concentrations. In this situation, the unprocessed product presently includes roughly 1 wt% Y_2O_3. Powder B1 exhibits a distinct tetragonal stage, while powders B2.5, B5, as well as B20 exhibit a combination of tetragon as well as cuboid stages. B20 powder exhibits a clearer division of (002) and (220), as

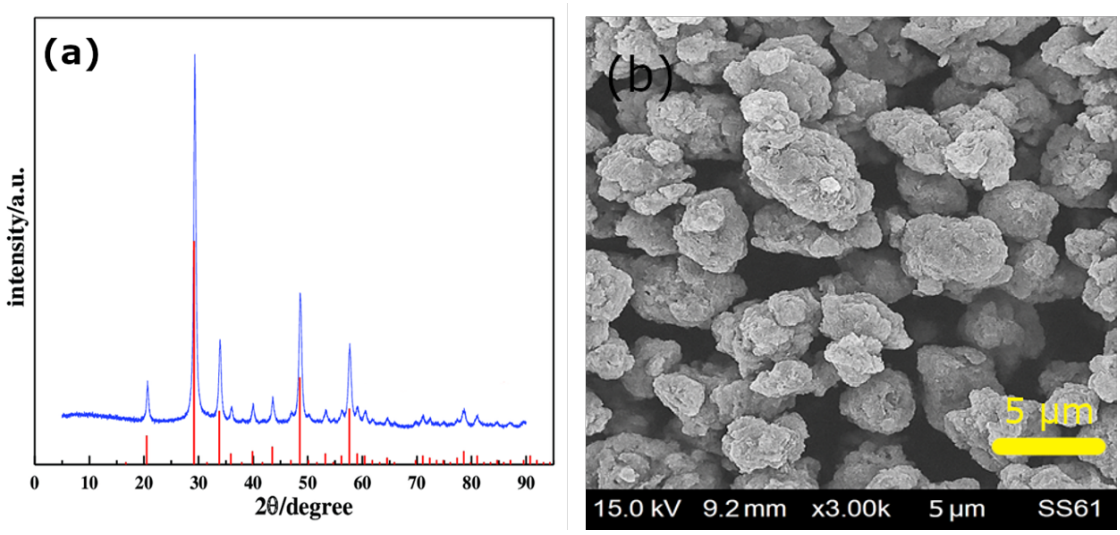

Figure 1. Characterization Data of Y_2O_3: (a) XRD, (b) SEM

Table 1. Result Comparison of Scattering Coefficients Influenced by Particle Sizes of Scattering Materials

Scattering materials	Scattering coefficients (mm^{-1})	Reduced scattering coefficients (mm^{-1})	References
Y_2O_3	10.11	0.53	This work
$CaCO_3$	8.96	0.15	(Tung et al., 2024b)
SiO_2	9.16	0.78	(Le et al., 2024)
KBr	42.5	13.5	(Anh, 2024)
MgO	3.54	0.059	(Loan and Anh, 2021)

well as a lower angle of the (111) maximum compared to powders B2.5 and B5. In contrast to the A specimens, only the powder B20 shows Y_2O_3 maxima, indicating that the majority of it remains in the form of an individual oxide. Furthermore, in the case of B20, three more maxima arise among 2θ = 29.5 - 30°. They differ from the $BaTiO_3$ or the Y_2O_3 stages. The extra Y_2O_3 may interact with the $BaTiO_3$ matrix and other additional substances, leading to these results. Given the possibility of secondary stages forming when the soluble amount of Y_2O_3 exceeds the limits of 1.5 at% (Ba-site) as well as 12.3 at% (Ti-site), a screening for subsequent stages was performed, yielding an association with $Ba_6Ti_{17}O_{40}$. $BaTiO_3$ and TiO_2 typically form a eutectic, however with SiO_2, the temperature drops. In the absence of a liquid state (Tang et al., 2022; Anh and Lee, 2024), the relationship among doped substances and additional substances can result in a Ti-rich stage, generating the subsequent stage $Ba_6Ti_{17}O_{40}$. This additional stage has been described before (Tung et al., 2024b,a).

Ceramic units are made via sintering non-doped as well as doped powders, BT-A and BT-B, under the circumstances stated in the preceding part. It exhibits the ceramics' X-ray scattering structures. Y_2O_3 has a higher effect on the $BaTiO_3$ composition in ceramics. The XRD structure from the B1 powder shows no maximum dividing, showing a stage transition from tetragonal to cubic. The similar effect is seen with B2.5 and B5 ceramics. This trend demonstrates a powerful relationship among additional substances and doped substances introduced to $BaTiO_3$. The inclusion of Y_2O_3 changes the $BaTiO_3$ form, which appears in the ceramic densificating process. Even while densificating process declines with increasing Y_2O_3 content for every case (BT-A as well as BT-B), ceramics produced from BT-B powder exhibit greater densificating rates. This is understandable given that one of the functions of the chemicals put into the $BaTiO_3$ powder is to boost its density.

Figure 2 illustrates the relationship between Y_2O_3 dosage and light dispersion, with Figure 2(a) showing dosage range from 1 to 10 μm, Figure 2(b) showing dosage range from 11 to 20 μm, Figure 2(c) showing dosage range from 1-5 μm under angles, Figure 2(d) showing dosage range from 6-10 μm under angles, Figure 2(e) showing dosage range from 11-15 μm under angles, Figure 2(f) showing dosage range from 16-20 μm under angles. It improves light transmission and wavelength conversion efficiency, resulting in enhanced Y_2O_3 levels. Blue light dispersion from forward emission can be enhanced, while blue light brightness can be improved by lowering forward scattering and reabsorption. This is accomplished by increasing the concentration of Y_2O_3 while decreasing the concentration of yellow phosphorus. The ability to specify an acceptable

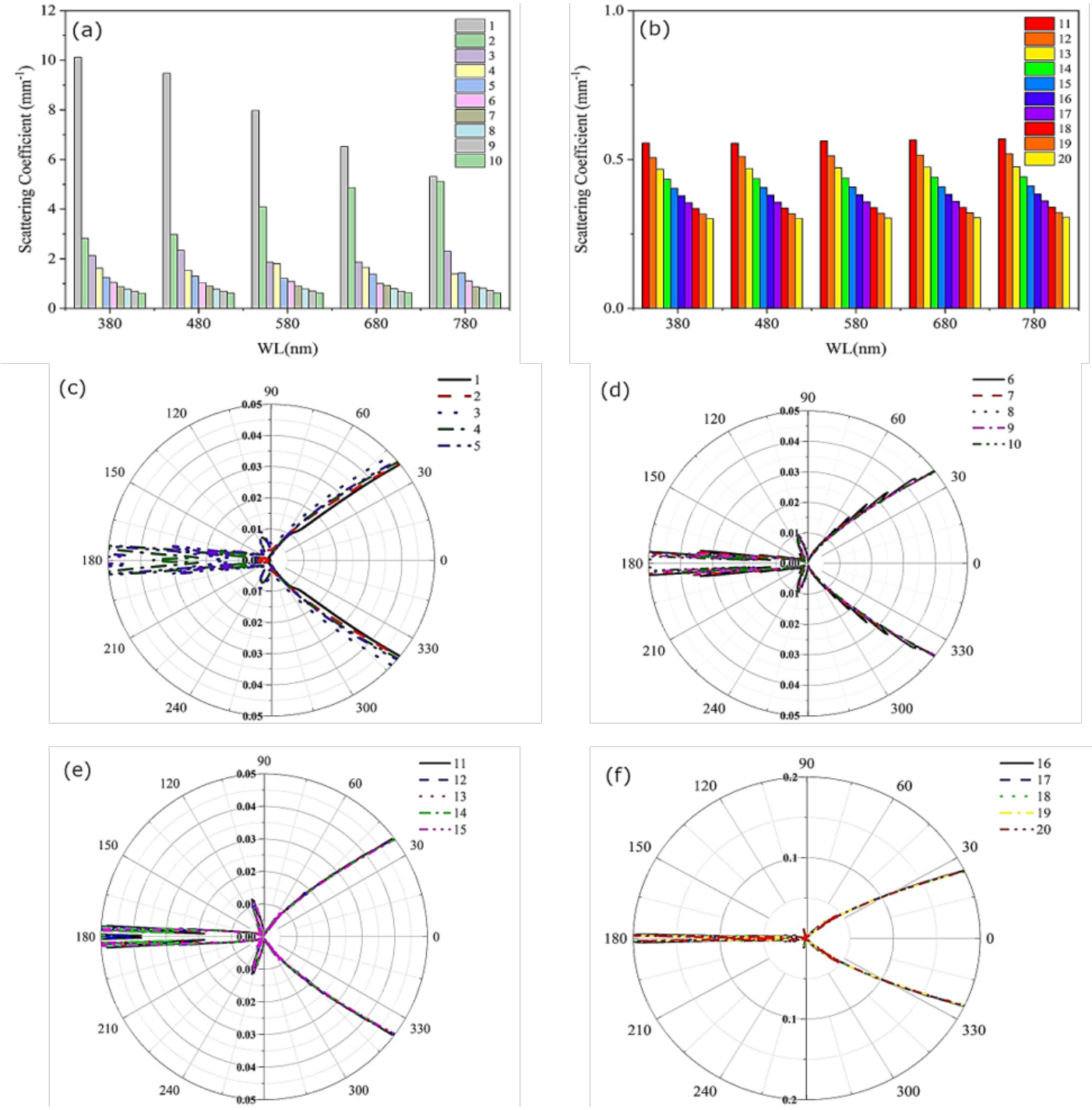

Figure 2. Scattering Factors with Various Particle Sizes: a) 1-10 μm, (b) 11-20 μm, (c) 1-5 μm Under Angles, (d) 6-10 μm Under Angles, (e) 11-15 μm Under Angles, (f) 16-20 μm Under Angles

color temperature (CCT) is likewise limited. Figures 4 and 5 demonstrate that CCT is concentration independent, but Figure 3 demonstrates that when the Y_2O_3 dosage grows, so does the YGA:Ce yellow phosphor dosage. Figure 3 shows that as the Y_2O_3 dosage is raised (1-20 wt.%), the YGA:Ce phosphor ratio decreases from approximately 25.5% to nearly 27.5%. Phosphorus CCT variation decreases with increased doping, as displayed by Figure 4 with Figures 4(a), 4(b),4(c), 4(d) showing disparate doping ranges of 1-5%, 6-10%,11-15%, 16-20%, respectively. CCT values peak at over 3050 K for 12 wt.% Y_2O_3 composition and fall to the deepest point at under 3000 K for 11 wt.% Y_2O_3 composition. The D-CCT achieves

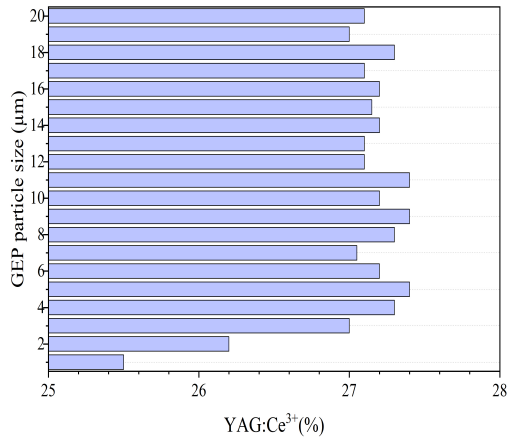

Figure 3. YGA:Ce Phosphor Proportion Values with Different Y_2O_3 Proportions

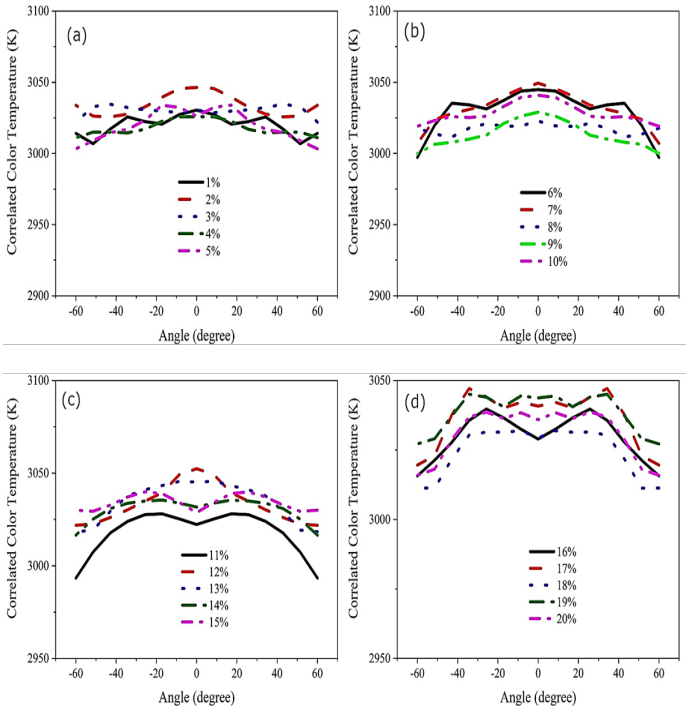

Figure 4. CCT Values with Various Y_2O_3 Proportions: (a) 1-5%, (b) 6-10%, (c) 11-15%, (d) 16-20%

minimum value under 15 wt.% Y_2O_3, being approximately 150 K smaller compared to the maximal outcome of 4 wt.% Y_2O_3, being approximately 170 K, as shown in Figure 5.

Y_2O_3 does not necessarily increase the brightness of white light emissions, as Figure 6 illustrates. A Y_2O_3 concentration of 19 weight percent produced the best results (over 74 lm), while a concentration of 1 weight percent produced the lowest results (just around 70.5 lm). Reduced blue emission and an uneven color distribution are the results of increased backscattering and reabsorption. Higher concentrations of Y_2O_3 can cause the phosphor to shift from blue to yellow or orange-red

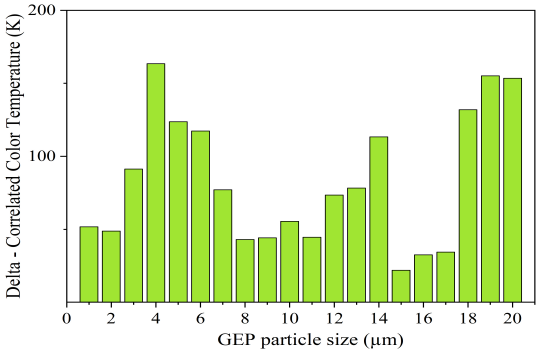

Figure 5. Color Difference Values with Different Y_2O_3 Proportions

when subjected to additional backscattered blue light. Only specific Y_2O_3 concentrations are suitable for the application of the phosphor coating. A shorter emission spectrum would arise from the many reflections caused by the changing light from different objects. As stated by Con et al. (2024) and Le et al. (2024), a high dosage of phosphor may improve the percentage of converted light reflected back, increasing CCT while lowering luminous intensity. Figure 6 illustrates how brightness and color uniformity are improved when 19 weight percent Y_2O_3 is added to a simulated WLED with a lumen output power of more than 74 lm. The impact of Y_2O_3 concentration on the brightness and color rendition of white LEDs is seen in Figures 7 and 8. When Y_2O_3 concentration rose to 20 weight percent, color rendition experiments using the color rendering indicator (CRI) and color quality scale (CQS) showed a discernible change. The erratic nature of blue, green, and yellow-orange may be the cause of the rise in CRI and CQS values. Increased dispersion, a bias toward the yellow-orange spectrum, and irregular light emission are the outcomes of high Y_2O_3 levels. We will modify this phosphor's CRI and CQS as we assess the outcomes, accounting for other elements such particle size. Table 1 presents the scattering coefficients and reduced scattering coefficients of various scattering materials. In this work, Y_2O_3 and $CaCO_3$ both show moderate scattering behavior, with coefficients of 10.11/0.53 mm^{-1} and 8.96/0.15 mm^{-1}, respectively. Compared with them, SiO_2 (Le et al., 2024) demonstrates similar scattering strength (9.16/0.78 mm^{-1}), while KBr (Anh, 2024) shows much higher values (42.5/13.5 mm^{-1}), indicating strong scattering. In contrast, MgO (Loan and Anh, 2021) exhibits the lowest scattering coefficients (3.54/0.059 mm^{-1}), suggesting weaker light scattering capability. Overall, the results confirm that Y_2O_3 and $CaCO_3$ occupy an intermediate position between strong scatterers like KBr and weak scatterers like MgO.

Table 2 compares the optical performance of these scattering materials in YAG:Ce^{3+}-based white LEDs. Y_2O_3 from this work provides a YAG:Ce^{3+} conversion efficiency of 27.4%, a correlated color temperature (CCT) reaching 3000 K, as well as a low ΔCCT reaching 21.92 K, highlighting its excellent

Table 2. Comparative Tables of This Research Results with Reported Research

Scattering materials	YAG:Ce^{3+} (%)	CCT (K)	D-CCT (K)	CRI	CQS	Lumen (lm)	References
Y_2O_3	27.4	3000	21.92	56.31	4292	74.04	This work
$CaCO_3$	6	5000	183.21	56.57	61.52	161.63	(Tung et al., 2024b)
SiO_2	27.4	3000	30	56.3	42.5	73.7	(Le et al., 2024)
KBr	27.4	3000	35.4	56.2	42.4	73.7	(Anh, 2024)
MgO	14.5	4000	53.6	58.2	64.2	131.1	(Loan and Anh, 2021)

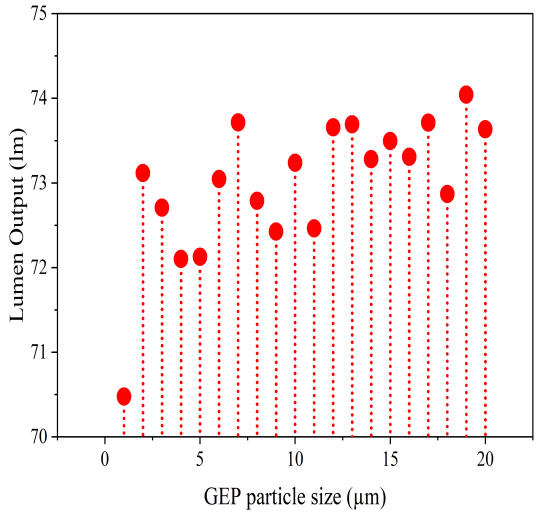

Figure 6. Luminescence Strength with Various Y_2O_3 Proportions

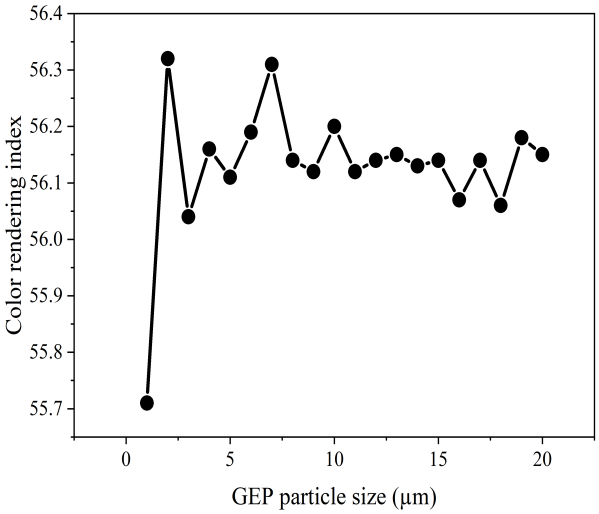

Figure 7. CRI Values with Various Y_2O_3 Proportions

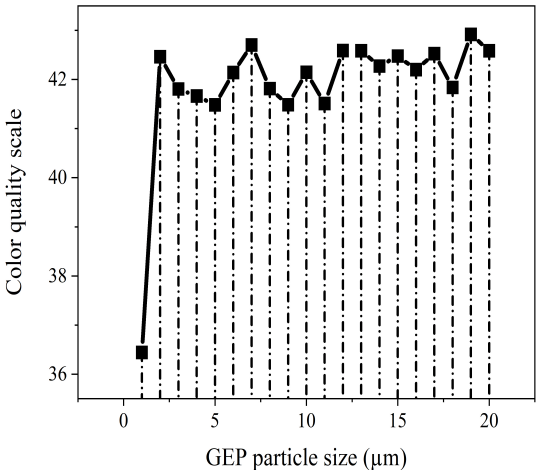

Figure 8. CQS Values with Various Y_2O_3 Proportions

color stability. Its luminous flux (74.04 lm), CRI (56.31), and CQS (42.92) are also comparable to SiO_2 (Le et al., 2024) and KBr (Anh, 2024), making it a strong candidate for stable performance applications. $CaCO_3$, on the other hand, delivers very high luminous flux (161.63 lm) and good color quality metrics (CRI = 56.57, CQS = 61.52), but at the expense of much poorer color stability (ΔCCT = 183.21 K). By contrast, MgO (Loan and Anh, 2021) also offers high luminous flux (131.1 lm) with good CQS (64.2), but suffers from a relatively large ΔCCT of 53.6 K.

Taken together, these findings emphasize the complementary strengths of Y_2O_3 and $CaCO_3$ in this work: Y_2O_3 stands out for its stability and balanced optical performance, while $CaCO_3$ is notable for its high brightness output despite significant color deviation. Compared with reported materials such as SiO_2, KBr, and MgO, the current study highlights that Y_2O_3 can serve as a reliable stable scatterer, whereas $CaCO_3$ can be leveraged in cases where brightness is prioritized over color uniformity.

4. CONCLUSIONS

Y_2O_3 was doped into clean and commercially manufactured $BaTiO_3$ powder using a typical solidifying process. Y_2O_3 was introduced unto clean $BaTiO_3$ as well as a commercial formula including 1 wt%, resulting in the last levels of 2.5, 5, as well as 20 wt%. The materials, both powder as well as ceramic units, were examined using XRD. When Y_2O_3 content increased, the impacts on $BaTiO_3$ composition became more apparent. The shift from tetragon towards a merger between tetragon as

well as cuboid phases can be seen in both heated powder and the resulting ceramics. In Y_2O_3-doped (20 wt%) commercially produced $BaTiO_3$ heated powder, an additional stage known as $Ba_6Ti_{17}O_{40}$ was reported to develop. There were no additional stages produced by $BaTiO_3$ and Y_2O_3, but the presence of free Y_2O_3 indicates that it has exceeded the soluble ability threshold. The modifications in the structure indicate that Y joined the structure, causing the creation of a subsequent stage free of Y and other formulating components. Because the experiments took place in air, the oxides were not lowered throughout the procedures.

5. ACKNOWLEDGMENT

The authors wishes to express their gratitude to the Posts and Telecommunications Institute of Technology, Vietnam, for financial support for this research.

REFERENCES

Alaizeri, Z. M., S. M. Ali, and H. A. Alhadlaq (2025). Enhancement of Photocatalytic and Anticancer Properties in Y_2O_3 Nanocomposites Embedded in Reduced Graphene Oxide and Carbon Nanotubes. *Catalysts*, **15**(10); 960

Anh, N. and H. Lee (2024). Titanium Dioxide in Vanadate Red Phosphor Compound for Conventional White Light Emitting Diodes. *Optoelectronics and Advanced Materials-Rapid Communications*, **18**(September-October 2024); 480–484

Anh, N. D. Q. (2024). Nano Scattering Particle: An Approach to Improve Quality of the Commercial LED. *Journal of Science and Technology*, **22**(3); 53–57

Anh, N. D. Q. and H. V. Ngoc (2020). Building Superior Lighting Properties for WLEDs Utilizing Two-Layered Remote Phosphor Configurations. *Materials Science-Poland*, **38**(3); 493–501

Con, P., L. Thuy, N. Loan, H. Lee, and N. a. Anh (2024). ZnO-Doped Yellow Phosphor Compound for Enhancing Phosphor-Conversion Layer's Performance in White LEDs. *Optoelectronics and Advanced Materials-Rapid Communications*, **18**; 389–395

Cong, P. and N. Anh (2025). Augmenting Chroma Performance for WLED Employing $Sr_8ZnSc(PO_4)$ 7: Eu^{2+}@SiO_2 as a Scattering-Enhancing Substance. *Science and Technology Indonesia*, **10**(2); 467–472

Dang, H. P., N. T. P. Loan, N. T. K. Chung, and N. D. Q. Anh (2021a). The Study of Convex-Dual-Layer Remote Phosphor Geometry in Upgrading WLEDs Color Rendering Index. *International Journal of Electrical and Computer Engineering*, **11**(5); 3890–3896

Dang, H. P., P. T. That, and N. D. Q. Anh (2021b). Utilizing $CaCO_3$, CaF_2, SiO_2, and TiO_2 Phosphors as Approaches to the Improved Color Uniformity and Lumen Efficacy of WLEDs. *TELKOMNIKA (Telecommunication Computing Electronics and Control)*, **19**(2); 623–630

Dang, N. H. S., D. M. T. Nguyen, T. P. L. Nguyen, D. Q. A. Nguyen, and H.-Y. Lee (2021c). Enhance wleds performance with additional phosphor materials in multi-layer remote structure. *Journal of Advanced Engineering and Computation*, **5**(3); 167–176

Hadi, D. S., H. Wafda, A. P. A. Mustari, V. Trisnawan, N. Widiawati, F. Miftasani, and D. H. Prajitno (2025). Corrosion Behavior of Modified F/M Steel with Ti and Dispersed Oxides: Y_2O_3 and ZrO_2 Under High Temperature in Static Liquid Lead. *Science and Technology Indonesia*, **10**(3); 877–888

Hou, B., X. Wang, R. Tang, W. Zhong, M. Zhu, Z. Tan, and C. Wang (2025). The Study on the Electrochemical Efficiency of Yttrium-Doped High-Entropy Perovskite Cathodes for Proton-Conducting Fuel Cells. *Materials*, **18**(15); 3569

Le, P., N. Anh, and H. Lee (2024). Regulating the White LED Properties with Different SiO_2 Particle Sizes. *Optoelectronics and Advanced Materials-Rapid Communications*, **18**(9-10); 485–489

Li, H., R. Pang, Y. Luo, H. Wu, S. Zhang, L. Jiang, D. Li, C. Li, and H. Zhang (2019). Structural Micromodulation on Bi^{3+}-Doped $Ba_2Ga_2GeO_7$ Phosphor with Considerable Tunability of the Defect-Oriented Optical Properties. *ACS Applied Electronic Materials*, **1**(2); 229–237

Li, Z., Y. Tang, J. Li, C. Wu, X. Ding, and B. Yu (2018). High Color Uniformity of White Light-Emitting Diodes Using Chip-Scaled Package. *IEEE Photonics Technology Letters*, **30**(11); 989–992

Limbu, S., L. R. Singh, and G. S. Okram (2020). The Effect of Lithium on Structural and Luminescence Performance of Tunable Light-Emitting Nanophosphors for White Leds. *RSC Advances*, **10**(59); 35619–35635

Lissner, I. and P. Urban (2011). Toward a Unified Color Space for Perception-Based Image Processing. *IEEE Transactions on Image Processing*, **21**(3); 1153–1168

Liu, Z.-Y., C. Li, B.-H. Yu, Y.-H. Wang, and H.-B. Niu (2012). Effects of YAG: Ce Phosphor Particle Size on Luminous Flux and Angular Color Uniformity of Phosphor-Converted White LEDs. *Journal of Display Technology*, **8**(6); 329–335

Loan, N. and N. Anh (2021). Enhancing Optical Performance of Dual-Layer Remote Phosphor Structures with the Application of $LaAsO_4$: Eu^{3+} and Y_2O_4: Ho^{3+}. *Optoelectronics and Advanced Materials-Rapid Communications*, **15**(1-2); 71–78

Ma, B., K. Ma, X. Qin, Y. Xi, J. Zhang, X. Yang, P. Yang, and W. Liu (2025). Effect of Hafnium-Based Thin Film Thickness on Microstructure and Electrical of Yttrium-Doped Hafnium Oxide Ferroelectric Devices Prepared by Magnetron Sputtering. *Micromachines*, **16**(9); 1066

Pham, V. T., N. H. Phan, G.-F. Luo, H.-Y. Lee, and D. Q. A. Nguyen (2021). The Application of Calcium Carbonate $CaCO_3$ and Titania TiO_2 for Color Homogeneity and Luminous Flux Enhancement in PC-LEDs. *Journal of Advanced Engineering and Computation*, **5**(2); 75–82

Rianjanu, A., T. Haloho, J. L. Pasaribu, A. G. Fahmi, E. Nurfani, W. S. Sipahutar, H. T. Yudistira, and T. Taher (2025).

Electrospun Rare-Earth Metal Oxide (CeO_2) Nanofiber for the Degradation of Congo Red Aqueous Dyes. *Science and Technology Indonesia*, **10**(1); 123–130

Shi, X., Y. Chen, G. Li, K. Qiang, Q. Mao, L. Pei, M. Liu, and J. Zhong (2023). Designing a Dual-Wavelength Excitation Eu^{3+}/Mn^{4+} Co-Doped Phosphors for High-Sensitivity Luminescence Thermometry. *Ceramics International*, **49**(12); 20839–20848

Tang, Q., N. Guo, Y. Xin, W. Li, B. Shao, and R. Ouyang (2022). Luminous Tuning in Eu^{3+}/Mn^{4+} Co-Doped Double Perovskite Structure by Designing the Site-Occupancy Strategy for Solid-State Lighting and Optical Temperature Sensing. *Materials Research Bulletin*, **149**; 111704

That, P. T. and N. Đ. Q. Anh (2021). Green $Ca_2La_2BO_{6.5}$: Pb^{2+} Phosphor: An Innovative Solution in Enhancing the Color Quality and Luminous Flux of WLEDs. *TELKOMNIKA (Telecommunication Computing Electronics and Control)*, **19**(5); 1630–1635

That, P. T., N. T. P. Loan, L. V. Tho, n. D. Q. Anh, H.-Y. Liao, G.-F. Luo, and L. Hsiao-Yi (2020). Enhancing Color Quality of WLEDs with Dual-Layer Remote Phosphor Geometry. *Materals Science Poland*, **38**(4); 667–74

Thi, M. H. N., P. T. That, and N. D. Q. Anh (2020). Eu^{2+}-Activated Strontium-Barium Silicate: A Positive Solution for Improving Luminous Efficacy and Color Uniformity of White Light-Emitting Diodes. *Materials Science-Poland*, **38**(4); 594–600

Thi, M. H. N., P. T. That, and N. D. Q. Anh (2021). The Impacts of Red-Emitting Phosphor $Mg_8Ge_2O_{11}F_2$: Mn^{4+} on the Color Rendering Index of Convex-Dual-Layer Remote Phosphor WLEDs at 5600 K. *TELKOMNIKA (Telecommunication Computing Electronics and Control)*, **19**(3); 950–956

Thuy, L. X., H. T. Tung, L. T. Dat, and N. L. M. Nhan (2025). Performance of ZnS and ZnSE Doped on Cu^{2+} for Photovoltaic Devices. *Science and Technology Indonesia*, **10**(3); 952–957

Tung, H., B. Minh, N. Thai, H. Lee, and N. Anh (2024a). ZnO Particles As Scattering Centers to Optimize Color Production and Lumen Efficiencies of Warm White LEDs. *Optoelectronics and Advanced Materials-Rapid Communications*, **18**; 283–288

Tung, H. T., N. T. P. Loan, and N. D. Q. Anh (2024b). The Enhancement Chromatic Uniformity and Illuminating Flux of WLEDs with Dual-Layer Phosphorus Configuration. In *International Conference on Advanced Engineering Theory and Applications*. Springer, pages 167–174

